Formation of Copper Zinc Tin Sulfide Thin Films from Colloidal Nanocrystal Dispersions via Aerosol-Jet Printing and Compaction

Bryce A. Williams, Ankit Mahajan, Michelle A. Smeaton, Collin S. Holgate, Eray S. Aydil,* and Lorraine F. Francis*

Department of Chemical Engineering and Materials Science, University of Minnesota, Minneapolis, Minnesota 55455, United States

S *Supporting Information*

ABSTRACT: A three-step method to create dense polycrystalline semiconductor thin films from nanocrystal liquid dispersions is described. First, suitable substrates are coated with nanocrystals using aerosol-jet printing. Second, the porous nanocrystal coatings are compacted using a weighted roller or a hydraulic press to increase the coating density. Finally, the resulting coating is annealed for grain growth. The approach is demonstrated for making polycrystalline films of copper zinc tin sulfide (CZTS), a new solar absorber composed of earth-abundant elements. The range of coating morphologies accessible through aerosol-jet printing is examined and their formation mechanisms are revealed. Crack-free albeit porous films are obtained if most of the solvent in the aerosolized dispersion droplets containing the nanocrystals evaporates before they impinge on the substrate. In this case, nanocrystals agglomerate in flight and arrive at the substrate as solid spherical agglomerates. These porous coatings are mechanically compacted, and the density of the coating increases with compaction pressure. Dense coatings annealed in sulfur produce large-grain (>1 μm) polycrystalline CZTS films with microstructure suitable for thin-film solar cells.

KEYWORDS: *copper zinc tin sulfide, aerosol-jet printing, thin-film solar cell, nanocrystal, nanoparticle coating, spray coating*
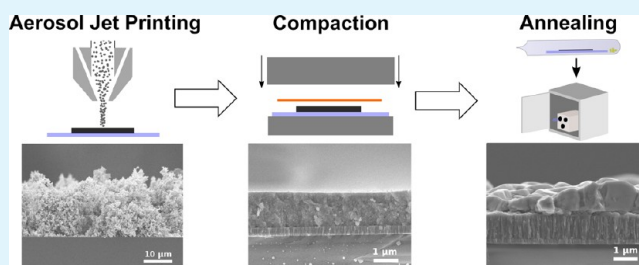
1. INTRODUCTION

Forming the light-absorbing layers in thin-film solar cells using a liquid-based continuous roll-to-roll processing approach may decrease module manufacturing costs and increase production throughput.[1,2] A variety of different liquid-based film deposition methods compatible with roll-to-roll production have been reported and used for making CdTe, CuInGaSe$_2$ (CIGS), and Cu$_2$ZnSnS$_4$ (CZTS) solar cells. These methods include coating from particle dispersions,[3−6] deposition from molecular precursor solutions,[7] spray pyrolysis,[8] and electrochemical deposition.[9,10] CZTS in particular has received increasing research interest because it comprises earth-abundant and nontoxic elements. Moreover, it has a very high absorption coefficient (>10^4 cm^{-1} in the visible wavelength range),[7] and its band gap can be tuned between 1 and 1.5 eV, the optimum range for solar cells, through Se incorporation (i.e., Cu$_2$ZnSn(S$_{1−x}$Se$_x$)$_4$).[11]

CZT(S,Se) films made by annealing coatings cast from nanoparticle dispersions and molecular precursor solutions have been used to make solar cells with power conversion efficiencies as high as 9.0[12] and 12.6%,[13] respectively. The highest efficiencies have been achieved by Wang et al.[13] through the use of hydrazine-based metal inks as precursors to CZT(S,Se). This approach benefits from solution processability, but scale-up is complicated by the toxicity and flammability of hydrazine. In an alternative method, colloidal nanocrystal dispersions replace the hydrazine-based molecular inks. In both approaches, the precursor coating is annealed at ~500−600 °C in S or Se vapor to achieve polycrystalline films with micrometer size grains suitable for solar cells. In fact, this general strategy has also been used to make CdTe, CIGS, and CZT(S,Se) thin films and solar cells.[12,14,15]

Ink-based film formation methods have several advantages, including the separation of the synthesis step from the coating process to achieve better stoichiometric uniformity, ease of integration with continuous roll-to-roll processing, and high-throughput production.[1] Nevertheless, there are several difficulties that complicate the large-scale continuous production of films from nanocrystal dispersions (hereafter also referred to as inks). Cracking of nanocrystal coatings during drying and long drying times are two important issues that must be addressed.[16−18] Nanocrystal coatings crack to relieve capillary stresses during drying.[19] Moreover, stresses can build because of constrained shrinkage during annealing; films shrink when dispersion stabilizing ligands desorb or decompose during heating. Because of these effects, it is difficult to deposit micrometer-thick coatings from dispersions of nanocrystals with sizes <10 nm in a single step and within the constraints of solar-cell manufacturing requirements.

Several strategies have been used to prevent cracking. In one strategy, polymer binders are added to the nanocrystal dispersion to increase the film toughness. Although this approach has produced crack-free films, solar cells made from these films suffered from low power conversion efficiencies.[20,21] Cracking can also be avoided if the coating is thinner than the critical cracking thickness (CCT).[19,22] To circumvent cracking, thick coatings are prepared by depositing multiple layers through spin-coating or dip-coating, where each layer is thinner than the CCT.[3,4,23] Intermediate heating and/or chemical treatments may be necessary to prevent the coating from redispersing during the next layer deposition.[23]

Herein, a general method to create dense, micrometer-thick, crack-free coatings is demonstrated with CZTS nanocrystals. Additionally, the CZTS nanocrystal coatings can be annealed to form polycrystalline CZTS films with microstructure suitable for solar cells. The approach to forming polycrystalline films comprises three steps: aerosol-jet printing (AJP) from dispersions of CZTS in toluene, densification by compression, and annealing in sulfur vapor. AJP (or spray deposition) combined with the compaction step can be used with nanoparticles other than CZTS, particularly when a high-throughput continuous process is required to form dense nanoparticle coatings. Combining these steps with post annealing can produce a wide range of inorganic polycrystalline films.

2. EXPERIMENTAL SECTION

2.1. Materials. Metal diethyldithiocarbamate precursors used for nanocrystal synthesis were synthesized as described by Chernomordik et al.[24] Octadecene (technical-grade, 90%), oleic acid (technical-grade, 90%), oleylamine (technical-grade, 70%), and toluene (HPLC-grade, 99%) were purchased from Sigma-Aldrich. Reagent alcohol (histological-grade, 90% ethyl alcohol, 5% methyl alcohol, 5% butyl alcohol) and acetone (HPLC-grade, 99.5%) were purchased from Fisher Scientific. Isopropyl alcohol (histological-grade, 99.5%) was purchased from Macron Fine Chemicals. Silicon (test-grade), fused-quartz polished plates, Kapton, and soda-lime glass substrates were purchased from Silicon Quest International, GM Associates, American Durafilm, and Valley Design Corporation, respectively. Solid sulfur (99.999%) was purchased from Cerac, Inc.

2.2. Nanocrystal Dispersions. Copper zinc tin sulfide (Cu_2ZnSnS_4) nanocrystals were synthesized via the hot-injection method from metal diethyldithiocarbamate precursors in a manner similar to that described by Khare et al. and Chernomordik et al.[5,24] Briefly, copper(II) diethyldithiocarbamate (108.6 mg), zinc(II) diethyldithiocarbamate (56 mg), and tin(IV) diethyldithiocarbamate (106.8 mg) precursors were dissolved in a solution of 36 mL of octadecene and 4 mL of oleic acid in a 100 mL round-bottomed flask. The solution was degassed under vacuum and then purged using nitrogen; this degas−purge cycle was repeated three times. The precursor solution was then heated to 175 °C. After reaching 175 °C, 1 mL of oleylamine was quickly injected into the precursor solution through a rubber septum. The resulting solution was heated to and maintained at 175 °C for 10 min. Following, it was cooled to room temperature by immersing the flask in a cold-water bath. The cooled solution was diluted with reagent alcohol at a 1:1 volume ratio and centrifuged to sediment the CZTS nanocrystals. After decanting the supernatant, the nanocrystals were dispersed in 4 mL of toluene. The sedimentation and redispersion procedure was repeated twice to remove residual reactants and any nonvolatile reaction products from the solution. Following synthesis, the nanocrystals were dispersed in 5 mL solution of oleic acid (10^{-4} volume fraction) in toluene. Before use, the nanocrystal dispersion was diluted with toluene and oleic acid solution to produce a 1−5 wt % CZTS dispersion. The average diameters of the CZTS nanocrystals used in this study were between 4 and 5 nm as determined from the width of the (112) X-ray diffraction

peak using the Scherrer equation. This 1 nm range is due to variations between numerous batches used in the study.

2.3. Aerosol-Jet Printing. AJP is a direct-write method for patterning functional materials on substrates for a variety of applications, such as printed electronics,[25−27] solar cell metallization,[28] and organic photovoltaics.[29] Figure 1 shows a schematic of the AJP
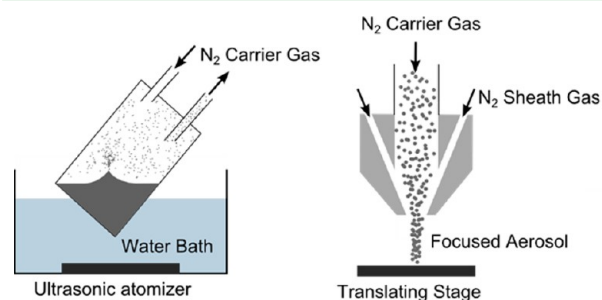

Figure 1. Schematic of the aerosol-jet printing system used for coating substrates with CZTS nanocrystals; atomizer is on the left; nozzle is on the right.

process. An aerosol mist composed of ∼1−5 μm dispersing liquid (toluene) droplets containing the nanocrystals is created by agitating the ink in an ultrasonic atomizer with adjustable wave amplitude. The vial containing the ink is immersed in a cooling water bath to maintain a constant temperature. The aerosol is transported from the ultrasonic atomization vial to the jet nozzle by a carrier gas, typically dry nitrogen. At the nozzle, the aerosol stream is focused by a second nitrogen gas flow (the sheath gas), forming a high-speed jet with a velocity between 20 and 70 m/s, depending on the sheath and the carrier gas flow rates. The focusing ratio, F_R, relates these two flow rates and is defined as

$$F_R = \frac{Q_{SG}}{Q_{CG}} \tag{1}$$

where Q_{SG} and Q_{CG} are the sheath and the carrier gas flow rates, respectively.[30] Substrates are coated by placing them on an $x-y$ translation stage below the nozzle in the path of the aerosol jet. By rastering the stage and partially overlapping consecutive lines, coatings can be formed from the individual ∼200 μm wide lines. AJP is utilized here as a small-scale analog to a spray-deposition system that would create large area coatings more effectively.

Substrates, including silicon (used as-purchased with native SiO_2 layer), quartz, Kapton, and molybdenum-coated soda-lime glass (∼500 nm molybdenum layer formed by sputter deposition) were cleaned with isopropyl alcohol and acetone under ultrasonic sonication and dried using flowing nitrogen before use. After cleaning, the substrates were coated with CZTS nanocrystals using a commercial aerosol-jet printer with an ultrasonic atomizer (Aerosol Jet 200, Optomec Inc.). The ultrasonic atomizer produces droplets with diameters in the 1−5 μm range as reported by Optomec Inc. The vial containing the CZTS ink was immersed in a bath maintained at 19 °C with recirculating water. Dry nitrogen gas (HP-grade, 99.998%) was used as the carrier and sheath gases. Carrier and sheath gas flow rates were varied between 18−24 and 18−72 standard cubic centimeters per minute (sccm), respectively. The current supplied to the ultrasonic atomizer (U_A) was varied between 0.31 and 0.45 mA through the control system. Both 150 and 200 μm diameter nozzles were used. CZTS coatings are formed by rastering the stage to create 40 lines (each 11 mm long) with a center-to-center separation of 0.05 mm at a nozzle separation distance (end of nozzle to top of substrate) of 0.5 cm. Stage translation speeds (u_s) were varied from 1 to 8 mm/s.

Thermogravimetric analysis (PerkinElmer TG/DTA 6300) was carried out on the material exiting the aerosol-jet printer at carrier gas flow rate of 20 sccm and sheath gas flow rate of 36 sccm. A CZTS nanocrystal coating was created inside an aluminum TGA sample pan by rastering a 150 μm nozzle over a $3 \times 3\ mm^2$ area with 10 consecutive passes. During analysis, the temperature was ramped at 15
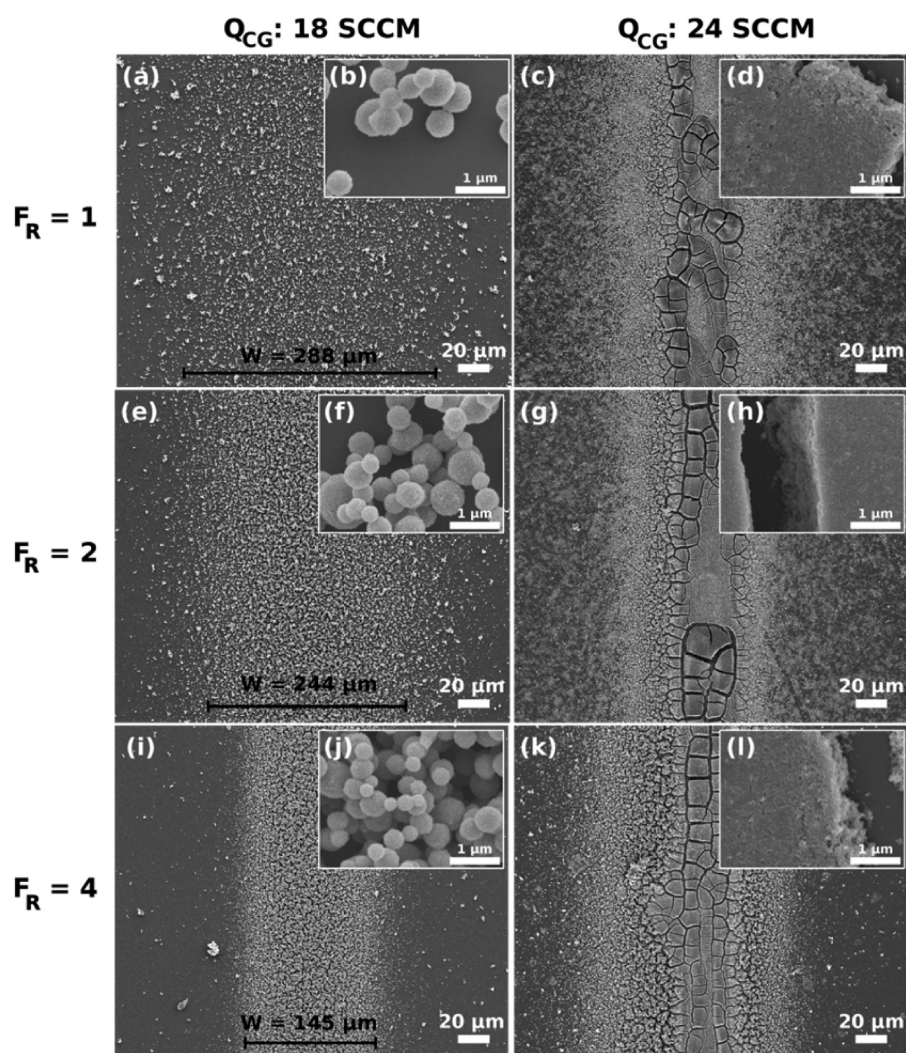
Figure 2. SEM images of isolated lines printed from 2 wt % dispersions of 5 nm CZTS nanocrystals. Coatings were printed on silicon substrates using carrier gas flow rates (Q_{CG}) of 18 sccm (a and b, e and f, i and j) and 24 sccm (c and d, g and h, k and l) with focusing ratios (F_R) of 1 (a−d), 2 (e−h), and 4 (i−l). Coatings were printed using a 150 μm nozzle at a stage speed u_s = 4 mm/s and atomization current U_A = 0.38 mA.

°C per minute from 25 to 140 °C and held at 140 °C for 15 min under a nitrogen gas purge before naturally cooling.

2.4. Coating Compression. Two compression methods, a weighted roller and a hydraulic press, were used for compacting the coatings. In compaction by the weighted roller, the nanocrystal coatings were compressed by passing them through a nip formed between a 1 cm diameter glass cylinder and a smooth glass plate mounted onto a raised metal platform. A schematic of the roller compression setup is shown in Figure S1 in the Supporting Information, accompanied by a full description of the apparatus setup and operation. Compaction pressures were adjusted by altering the weight loaded onto a steel platform suspended from the axle through the glass cylinder underneath the compaction platform (see Figure S1b in the Supporting Information). Compaction pressure was varied from 8 to 43 MPa by altering the weight suspended from the glass cylinder from 0.3 to 1.5 kg. The coated substrate was fixed on top of a polyethylene terephthalate (PET) film using a double-sided tape. A thin sheet of Kapton was placed over the coating to prevent the coating from sticking to the glass roller and to avoid subsequent delamination. The coated substrate was passed underneath the weighted roller by pulling the PET film at a steady rate (∼0.2 cm/s); the total compression time was approximately 5 s for the 1 cm long CZTS coating.

A hydraulic press (Carver AutoPellet 3887) was used to compress the CZTS nanocrystals at pressures higher than 50 MPa. The load

used during compression ranged from 450 to 5440 kg, corresponding to compaction pressures of 100 MPa to 1 GPa on the basis of the coating area. Because of deformation of the cover layer during compression, contact between the cover layer and coating substrate occurred outside of the coating, increasing the effective contact area and decreasing the actual compaction pressure by up to a factor of two. For this reason, the calculated pressures may not represent the true compaction pressures but are used as references to analyze the effect of increasing compaction load.

Coatings were compressed using two different methods. (See the Supporting Information for further details.) In the first method, the CZTS coatings were printed on to Kapton and then transferred onto a silicon substrate by placing the coated Kapton on top of the silicon with the CZTS coating facing the silicon. The nanocrystal coating, now sandwiched between the Kapton and the silicon substrate, was compressed for 60 s at the desired pressure. After compression, the Kapton layer was peeled from the nanocrystal coating, releasing and leaving the CZTS nanocrystals on top of the silicon substrate. This approach with the sacrificial Kapton layer was ineffective when molybdenum-coated soda-lime glass (Mo-coated SLG) substrates were used instead of silicon; the nanocrystals peeled with the Kapton layer and CZTS coating delaminated. To eliminate delamination from Mo-coated SLG substrates, a second hydraulic compression method was developed. In the second method, CZTS coating was printed on Mo-coated SLG instead of Kapton and then heated on a hot plate for 10
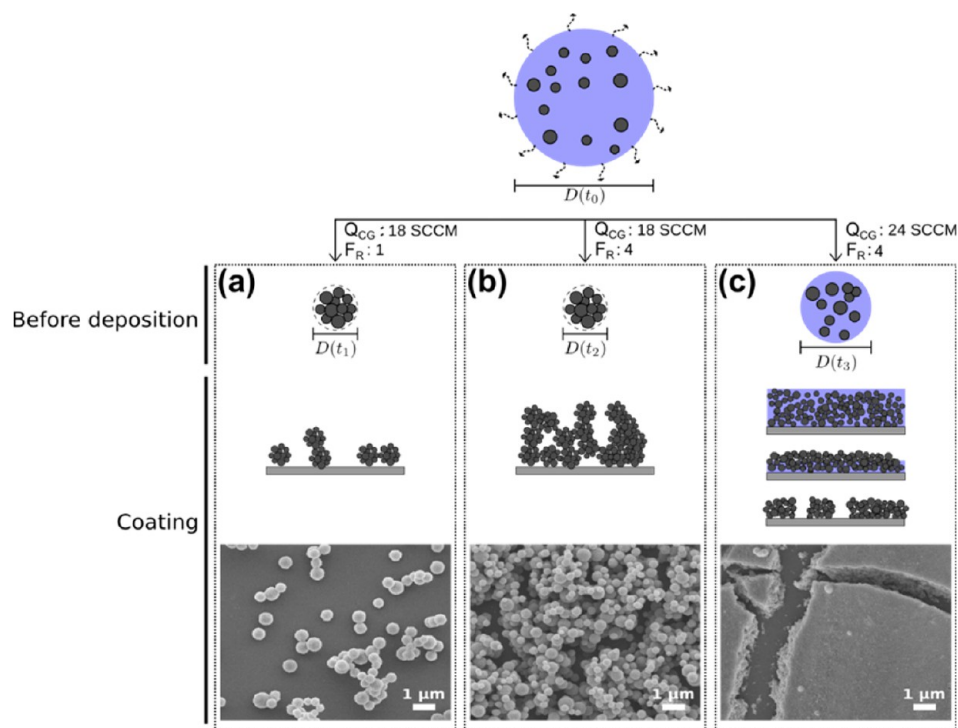
Figure 3. Illustrations of the aerosol drying process and the mechanisms that lead to various coating morphologies at various carrier gas flow rates, Q_{CG}, and focusing ratios. Upon atomization at $t = t_0$, a typical aerosolized nanocrystal dispersion droplet with an initial diameter $D(t_0)$ is transported by the carrier gas to the substrate. Transport times are inversely related to Q_{CG} so that $t_1 = t_2 > t_3$ in panels a through c. When Q_{CG} is 18 sccm (panels a and b), agglomerates form because the transport time is much longer than the time required for the solvent to evaporate. When Q_{CG} is 18 sccm and focusing ratio is 1, a sparse coating of agglomerates are deposited on the substrate. Increasing the focusing ratio to 4 produces a coating with higher coverage by these agglomerates. When the Q_{CG} is 24 sccm (panel c), agglomerates do not form because the transport time is too short for solvent to evaporate. Consequently, the nanocrystal dispersion droplet with diameter $D(t_3)$ arrives at the substrate surface with a significant amount of solvent. The liquid droplets with the nanocrystals coalesce after impinging the substrate, forming a wet dispersion coating, which then cracks upon drying.

min at temperatures ranging from 100 to 140 °C. This mild heat treatment was found to increase adhesion to the substrate if the annealing temperature was ≥120 °C. The heat-treated coatings were then compressed with a Kapton cover layer on top of the CZTS nanocrystals with no coating delamination, resulting in intact, compressed CZTS coatings even on Mo-coated SLG.

2.5. Annealing and Characterization. After compaction, the nanocrystal coatings on Mo-coated SLG were annealed using the method described by Chernomordik et al.[31] Briefly, the compacted nanocrystal coatings (area = 0.4 cm^2) were placed in quartz ampules with 1 mg of sulfur. Then, the ampule was evacuated to ~10^{-6} Torr and flame-sealed. The sealed ampule was loaded into a furnace preheated to 600 °C. After 1 h at 600 °C, the furnace was turned off. The ampules and the furnace were allowed to cool naturally to room temperature before removing the ampules from the furnace. The natural cooling rate was such that it took approximately 3 h before the ampule and the furnace cooled to 350 °C.[31]

The as-printed nanocrystal coatings and the annealed films were examined by scanning electron microscopy (JEOL-6500). The nanocrystal coatings and the annealed films, except those coated on Mo-coated SLG substrates, were coated with 3 nm of platinum to eliminate charging during imaging. Nanocrystal coating and film thicknesses were determined from cross-sectional SEM micrographs using image analysis software (NIH ImageJ). Average coating thicknesses of roller-compacted coatings were calculated from cross-sectional SEM images (×700 magnification) by averaging coating thickness measurements taken at 100 pixel intervals over the width of a 1280 × 1028 resolution image (coating width = 1.7 μm). The coatings and the annealed films were characterized using X-ray diffraction (XRD, Bruker D8 Discover) and Raman scattering (Witec Alpha300R) as described by Chernomordik et al.[31] and Johnson et al.[32] XRD and Raman spectra were collected from nanocrystals

deposited on Mo-coated SLG substrates before and after thermal annealing.

3. RESULTS AND DISCUSSION

3.1. Aerosol Jet Printing. Figure 2 shows CZTS nanocrystal lines created by AJP using carrier gas flow rates of 18 and 24 sccm with focusing ratios of 1, 2, and 4. A single line for each condition is shown to illustrate the effects of these parameters on coating density, morphology, and width. (To make continuous coatings, partially overlapping lines are printed.) All lines in Figure 2 were printed from a 2 wt % CZTS dispersion in toluene with an atomizer current of 0.38 mA while the stage was moved under a 150 μm diameter nozzle in a single pass at 4 mm/s. Using an 18 sccm carrier gas flow at a focusing ratio of 1 creates a ~288 μm wide line. Higher magnification SEM images show that this line comprises nanocrystal agglomerates with sizes ranging from 0.2 to 1 μm (Figure 2b). Increasing the focusing ratio to 2 and 4 decreases the line width to 244 and 145 μm, respectively, without substantial change in the microstructure of the coating; the lines still comprise 0.2−1 μm nanocrystal agglomerates. When the carrier gas flow is increased to 24 sccm, nanocrystal agglomerates no longer appear in the center of the printed line, but rather are limited to the line's outer edges. A cracked nanocrystal coating is formed at the center where the aerosol jet impinges on the substrate. Increasing the focusing ratio from 1 to 4 at a carrier gas flow rate of 24 sccm produces no significant changes in the coating line width, hinting that the jet diameter and fluid dynamics are irrelevant in determining the

printed line width under these conditions. This observation suggests that the line width is dictated by liquid spreading after deposition.[30] Indeed, all coatings deposited at high carrier gas flow rates are cracked, consistent with the printed line having high liquid content at the time of deposition.

The systematic study of the aerosol-jet printing parameters shown in Figure 2 revealed three types of coating morphologies: (1) discontinuous low-coverage coatings consisting of sparse nanocrystal agglomerates (e.g., Figure 2a,b); (2) continuous high-coverage coatings, also consisting of nanocrystal agglomerates (e.g., Figure 2i,j), and (3) cracked coatings (e.g., Figure 2c,d,g,h,k,l).

Figure 3 shows a schematic of the proposed mechanisms that result in these three morphologies. A key parameter that determines the coating morphology is the aerosol transport time

$$\tau_T = \frac{A_x L}{Q_{CG}} \tag{2}$$

where A_x and L are the cross-sectional area and length of the tubing that carries the aerosol from the atomization vessel to the nozzle, respectively.

The volume fraction of the solvent in the aerosol droplet when it lands on the substrate is determined by the evaporation rate and the time it takes for the aerosol droplets to travel from the atomization vessel to the nozzle, the aerosol transport time (τ_T). As the aerosol is generated in the atomization vessel, CZTS nanocrystals become entrained in the aerosol droplets at a concentration assumed to be equal to that of the bulk dispersion. At low carrier gas flow rates (Q_{CG} = 18 sccm and τ_T = 5.2 s, Figure 3a), the aerosol transport time is long, and a significant fraction of the solvent in the mist droplets evaporates before the droplets reach the substrate. As the solvent evaporates and the nanocrystal concentration rises, the nanocrystals agglomerate within the droplet (Figure 3a,b). The periphery of the agglomerates comprising 5 nm CZTS nanocrystals appears smooth and densely packed when examined with SEM (resolution ≥8 nm). Moreover, the agglomerates appear spherical, suggesting that nearly all or a significant fraction of the solvent has evaporated such that the aerosol of dispersion droplets has been transformed into an aerosol of spherical agglomerates with very low liquid content.[33] Thus, the agglomerates are nearly dry when they reach the substrate (Figure 3a,b). In this study, agglomerates formed when the carrier gas flow rate was ≤20 sccm, corresponding to $\tau_T \geq$ 4.6 s. Werner et al. have also reported similar coating morphologies during aerosol-jet printing of silver nanoparticles. Werner et al. used a tube heater to heat the aerosol as it traveled toward the substrate.[25] In Werner's work, solvent evaporation upon heating also formed an aerosol of agglomerates with very low liquid content. In our work, the morphology consisting of the agglomerates was observed even without heating.

At the lowest focusing ratio (F_R = 1) and with low carrier gas flow rates (Q_{CG} = 18 sccm), the nanocrystal agglomerates sparsely coat the substrate and form a wide line, as shown in Figures 2a and 3a. Increasing the focusing ratio to 4 (Figures 2i and 3b) while maintaining the carrier gas flow rate at 18 sccm results in a narrower line because focusing the jet while keeping the material flow rate constant increases the agglomerate flux to the substrate, as illustrated in Figure 2a,e,i. As a consequence, coverage of the substrate with nanocrystal agglomerates also

increases. Thus, increasing the focusing ratio results in a continuous, albeit porous, line of nanocrystal agglomerates.

Increasing the carrier gas flow rate to 24 sccm while keeping the focusing ratio at 3 results in nanocrystal coatings with significant cracking (Figure 3c). At 24 sccm, the transport time, τ_T = 3.9 s, is evidently shorter than the time it takes the solvent to evaporate. Thus, the dispersion droplets are solvent-laden as they impinge on the substrate and coalesce to form a wet coating. On the basis of the porous morphology at the cracked edges, the coating does not seem to densify fully, indicating a low solvent volume fraction upon aerosol impingement at the substrate. Nevertheless, this coating develops stresses while drying and eventually cracks to relax these stresses.

The balance between the evaporation time to form agglomerates and the transit time is additionally influenced by the dispersion properties, especially the properties of the dispersing liquid. The addition of cosolvents, a common practice in aerosol-jet printing,[30] or the use of a different dispersing liquid may reduce or accelerate the evaporation rate depending on the volatility of the dispersing liquid(s) relative to toluene. The change in the evaporation rate would be expected to shift the ranges of the absolute carrier gas flow rates where each distinct morphology is observed but not to affect the morphology trends with increasing carrier gas flow rate. Knowledge of the evaporation time to form CZTS nanocrystal agglomerates from the aerosol droplets would provide a predictive parameter for coating morphology, which could be adjusted for different dispersing liquids. However, calculating the evaporation time is complicated and requires modeling of the changes in the toluene partial pressure during AJP as well as the nontrivial effects of agglomerate formation on the evaporation rate. Although such modeling is outside the scope of the present study, further research exploring the effects of these factors may lead to a coating process map to predict morphology on the basis of the ratio of the evaporation and transit times.

Of the three distinct morphologies shown in Figure 3, the continuous coating of agglomerates (Figure 3b) appears most suitable as a precursor for forming thin polycrystalline films for solar cells. The morphology with sparse coverage of agglomerates (Figure 3a) is clearly undesirable and so is the cracked coating in Figure 3c. However, the morphology in Figure 3b, although free of cracks, is very porous. Annealing this film may result in a film with many voids. To reduce the porosity, the films were compressed using two approaches: compression using a weighted roller and compression using a hydraulic press. A similar approach was used by Halme et al. to produce dense TiO_2 nanoparticle coatings from agglomerates formed during spray deposition onto a heated substrate.[34] For the compression studies, the coatings were prepared by aerosol-jet printing using 5 nm CZTS nanocrystal dispersions in toluene and rastering the aerosol beam to cover a 10 mm × 4 mm area.

3.2. Compaction by Weighted Roller. Figure 4 shows a CZTS nanocrystal coating before (Figure 4a) and after (Figure 4b,c) compaction by a weighted roller at 25 MPa (1.5 kg mass loading). There is a clear decrease in the porosity and surface roughness of the coating after compaction. The extent of compaction, α, was determined from the average coating thickness before and after compaction using
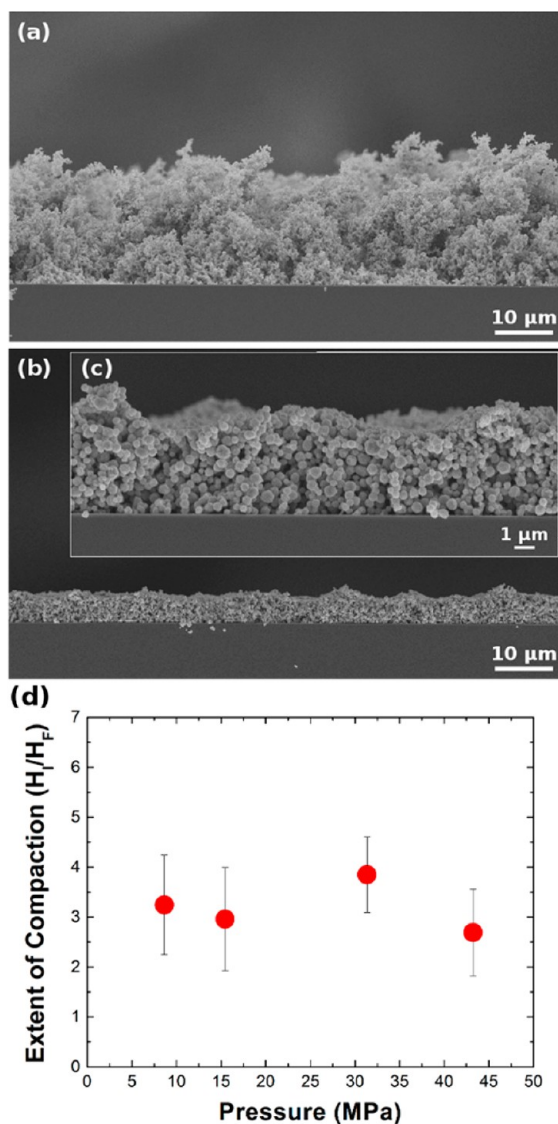
$$\alpha = \frac{H_I}{H_F} \tag{3}$$

Figure 4. Aerosol-jet-printed CZTS coating from a 2 wt % dispersion (a) before and (b and c) after compaction by a weighted roller at 44 MPa. Coatings were printed onto silicon substrates using a 150 μm nozzle, carrier gas flow rate Q_{CG} = 20 sccm, focusing ratio F_R = 3, stage speed u_s = 8 mm/s, and atomization current U_A = 0.38 mA. (d) Extent of compaction (initial coating thickness divided by final thickness) as a function of the compaction pressure.

where H_I and H_F are the initial (precompaction) and final (postcompaction) coating thicknesses, respectively. Figure 4d shows that within the range studied α is independent of compaction pressure. This indicates that the nanocrystal coating compacts into a dense agglomerate network readily and that this dense agglomerate network resists further consolidation and deformation. Additionally, there is no indication of agglomerate deformation at pressures accessible with the roller system (<45 MPa). Further decreases in porosity appear to require agglomerate deformation, which may be observed at the higher compaction pressures afforded by a hydraulic press.

3.3. Compaction by Hydraulic Press. Figure 5 shows an as-printed nanocrystal coating (Figure 5a,d) and coatings compacted at 200 MPa (Figure 5b,e) and 800 MPa (Figure 5c,f) using a hydraulic press. The compressed coatings were printed on Kapton and transferred onto silicon substrates. The

nanocrystal coating compacted at 200 MPa is clearly compressed, and the agglomerates have been flattened and deformed. The boundaries between the compressed agglomerates are still visible because the particles have not been compressed enough to form an entirely continuous coating. Increasing the pressure to 800 MPa deforms the agglomerates further, and the coating densifies significantly. The boundaries between the agglomerates are no longer visible in much of the coating. Occasional but infrequent voids (e.g., on the left edge of Figure 5c) are visible. These voids were also reported by Halme et al. in compaction of TiO$_2$ agglomerates; the authors thought that these voids formed in regions where there is not enough material to fill the voids between the agglomerates as they deform. The voids observed in this study are much smaller than the ~1−3 μm voids observed by Halme et al.[34]

The effect of mild annealing prior to compaction was investigated to improve adhesion to the coating substrate, particularly to molybdenum-coated substrates commonly used for CZTS solar cells. Figure 6a−d shows optical images of CZTS nanocrystal coatings on Mo-coated SLG substrates before (Figure 6a) and after compression by hydraulic press at 800 MPa following mild annealing at 100 °C (Figure 6b,c) and at 120 °C (Figure 6d). The as-printed coating completely covers the substrate and has a brown color. After mild annealing and compaction, the coatings appear darker. Mild annealing at 100 °C for 10 min does not prevent delamination (Figure 6b,c). The coating remains at the boundaries of the coating area, but CZTS nanocrystals at the center of the substrate peel and stick to the Kapton coverslip, as indicted with labels for the CZTS coating (C) and molybdenum (Mo) in Figure 6b,c. Increasing the annealing temperature above 120 °C (Figure 6d) eliminates delamination, producing dense coatings on Mo-coated SLG substrate. Figure 6e shows an SEM image of a CZTS nanocrystal coating on Mo-coated quartz substrate after annealing at 140 °C followed by compression at 800 MPa. Interestingly, CZTS coatings compressed without annealing (Figure 5c,f) appear to have higher coating density and fewer voids than coatings compressed after mild annealing at 120−140 °C, even when the compression pressures are the same. In addition to increasing coating adhesion, mild annealing increases the agglomerates' yield strength and resistance to deformation.

To understand the reason behind this observation, the CZTS nanocrystal agglomerates were studied using thermogravimetric analysis (TGA). Figure 6f displays the weight of the CZTS agglomerates and their temperature versus heating time. In this experiment, the agglomerates were heated to 140 °C at 15 °C/min and held at 140 °C for 15 min. During the analysis time, the CZTS agglomerates show a steady, linear weight loss for approximately 10 min. The total weight loss is 0.2 mg and corresponds to approximately 30% of the original weight. The onset of the weight loss corresponds to the normal boiling point of toluene (110 °C) and the reduction in weight is attributed to the evaporation of residual toluene trapped in the space between the CZTS nanocrystals within the agglomerates, likely still solvating and physically bound to the ligands surrounding the nanocrystals. This trapped toluene solvating the ligands is believed to have a lubricating effect during the compaction of the CZTS agglomerates. Presence of this toluene between the nanocrystals and the substrate weakens adhesion. Desorbing the residual toluene allows the coating to adhere better to the substrate. The agglomerates without the residual toluene (e.g., coatings after mild annealing) do not
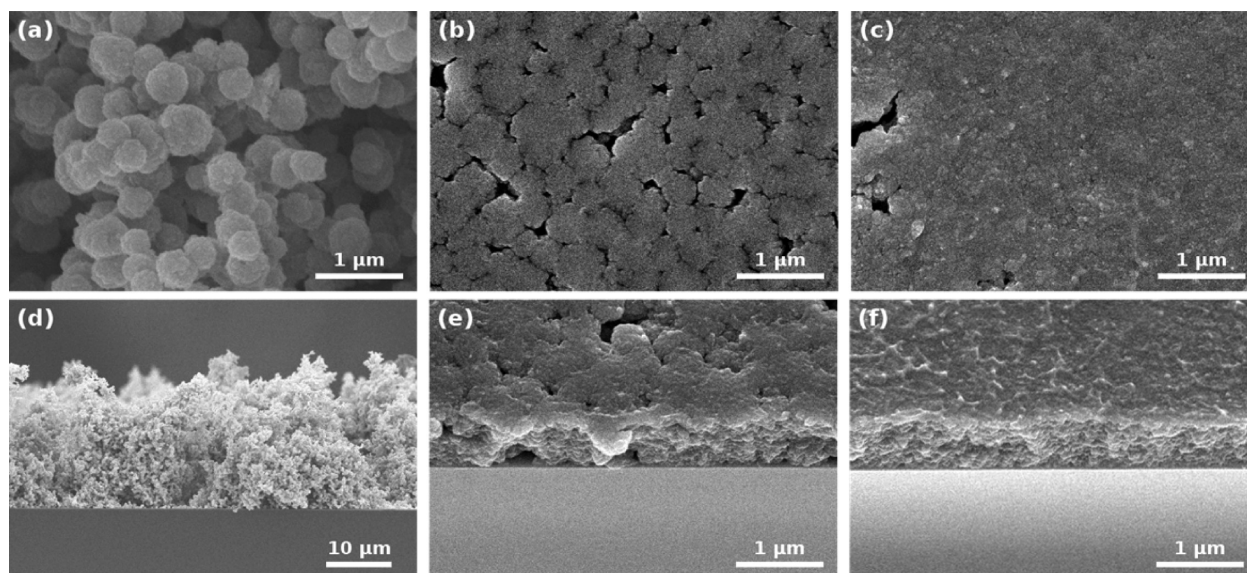
Figure 5. SEM images of aerosol-jet-printed coatings from a 2 wt % 5 nm CZTS nanocrystal dispersion (a and d) before and after compaction using a hydraulic press at 200 MPa pressure (b and e, respectively) and at 800 MPa (c and f, respectively). Coatings were printed on Kapton substrates using a 200 μm nozzle, carrier gas flow rate Q_{CG} = 20 sccm, focusing ratio F_R = 2.5, stage speed u_s = 4 mm/s, and atomization current U_A = 0.41 mA. At low compression pressures, 200 MPa, agglomerates deform, but the coating remains porous. Increasing loading to 800 MPa (c and f) deforms the agglomerates even more and forms a dense nanocrystal coating. Although there are still voids in the coating, these voids are limited in size and density.
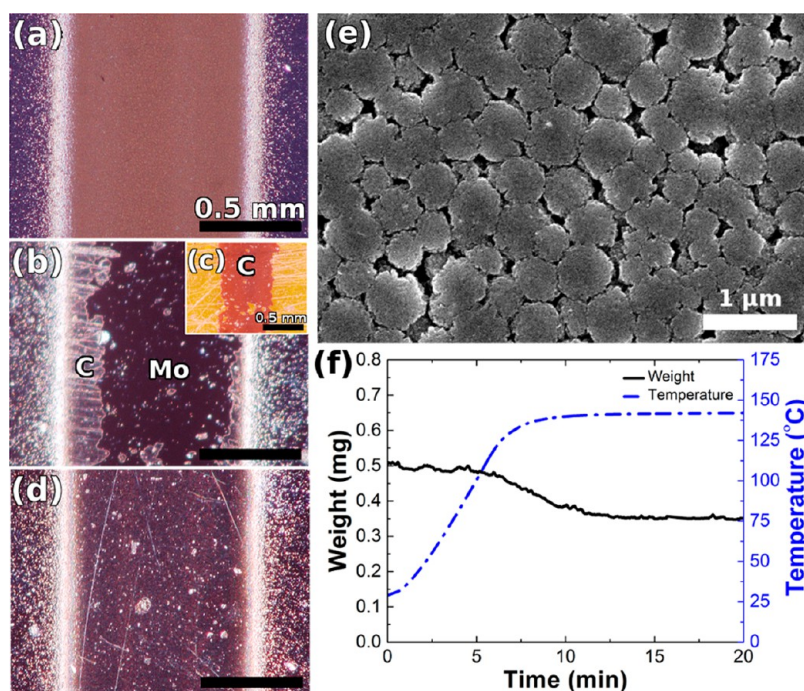

Figure 6. Optical images of CZTS nanocrystal coatings on Mo-coated SLG substrates formed via AJP (a) before and (b) after compression by a hydraulic press at 800 MPa following mild annealing (b and c) at 100 °C and (d) at 120 °C for 10 min. Panel c shows that heating at or below 100 °C did not prevent coating delamination and sticking to the Kapton cover layer; the coating, the region labeled as "C" at left edge of panel b, remains at the edges of the Mo-coated SLG substrate but is peeled off the substrate at center of the line that is attached to the Kapton (region labeled as "C" in center of panel c). Mild annealing treatments at or above 120 °C prevented delamination. (e) SEM image of a coating compressed at 800 MPa after annealing at 140 °C for 10 min. (f) TGA data from CZTS agglomerates heated to and held at 140 °C for 40 min. Significant weight loss occurs at approximately 5 min into analysis, corresponding to a temperature of 110 °C, near the boiling point of toluene.

deform as much as the agglomerates with residual toluene, but they still deform enough to increase the coating density.

3.4. Thermal Annealing of the Aerosol-Jet-Printed CZTS Nanocrystal Coatings.
Nanocrystal coatings prepared using the different approaches discussed above were annealed in sulfur vapor to transform them into polycrystalline thin films. Each coating has a distinct preanneal coating density that affects the final film morphology. The effect of coating density on the annealed film morphology is shown in Figure 7. Specifically, Figure 7a–d shows the SEM images of a CZTS film (Figure
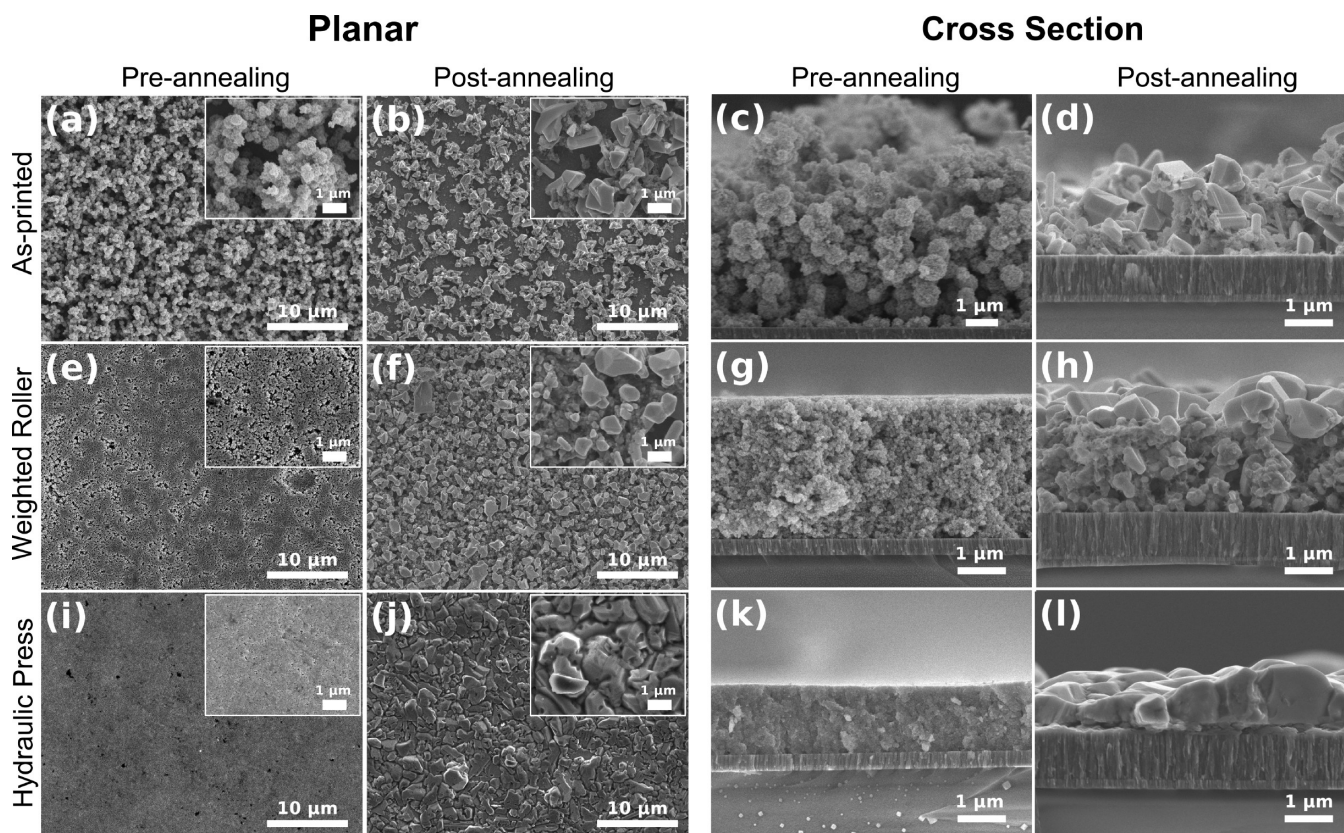
Planar

Pre-annealing · **Post-annealing**

Cross Section

Pre-annealing · **Post-annealing**

Figure 7. SEM images of CZTS nanocrystal coatings, compacted using different methods and compaction pressures, before and after annealing for 1 h at 600 °C with 1 mg of solid sulfur (~50 Torr) in the quartz ampule; (a−d) SEM images of a coating that was not compacted (a and c) before and (b and d) after annealing. (e−h) SEM images of a coating that was compacted using a weighted roller at 25 MPa (e and g) before and (f and h) after annealing. (i−l) SEM images of a coating compressed using hydraulic press at 800 MPa (i and k) before and (j and l) after annealing. Higher magnification planar SEMs are shown in the insets. All coatings were formed by AJP onto Mo-coated SLG substrates from a 5 wt %, 5 nm CZTS nanocrystal dispersion in toluene with a 150 μm diameter nozzle, carrier gas flow rate Q_{CG} = 20 sccm, focusing ratio F_R = 2.5, stage speed u_s = 1 mm/s, and atomization current U_A = 0.45 mA.

7b,d) made by annealing an as-printed nanocrystal coating without any compaction (Figure 7a,c). Figure 7e−h shows the SEM images of a CZTS film (Figure 7f,h) made by annealing a nanocrystal coating compacted at 25 MPa using the weighted roller (Figure 7e,g). Figure 7i−l show the SEM images of a CZTS film (Figures 7j,l) by annealing a nanocrystal coating compacted at 800 MPa using the hydraulic press (Figure 7i,k). Raman spectroscopy and XRD were also conducted on the annealed films and are shown in Figure S4 of the Supporting Information. These coatings were printed by AJP (Q_{CG} = 20 sccm, F_R = 1.8, u_s = 1 mm/s, U_A = 0.49 mA, 150 μm diameter nozzle) from a 5 nm CZTS nanocrystal dispersion (5 wt % in toluene) on Mo-coated SLG substrates. Under these printing conditions, nanocrystal agglomerates form during aerosol transport and coat the substrate with complete coverage as shown in Figure 3b. All coatings were annealed at 140 °C for 10 min. Two of the coatings were then compacted by weighted roller and hydraulic press. All three coatings were annealed for 1 h at 600 °C in 50 Torr of sulfur.[31]

Prior to annealing, the as-printed coating comprises submicrometer agglomerates that form a disordered porous coating. When this coating is annealed, 0.3−1 μm CZTS crystals form (e.g., Figure 7d), but the resulting film is discontinuous with some nanocrystal agglomerates, unaltered by annealing, interspersed in between the larger 0.3−1 μm grains. The coverage of large grains on the substrate is low with

significant empty spaces between them (Figure 7b). In addition to these empty spaces, there are large voids between the large grains even in locations where the grain density is high.

Annealing the coating that was compacted using a weighted roller at 25 MPa produces a denser film with fewer voids (Figure 7h), though careful inspection of SEMs from different locations still show occasional voids as large as 100 nm. Grains near the film surface are noticeably larger (>500 nm) than the grains closer to the substrate (<300 nm; Figure 7f,h). The large grains have an aerial density of 42 grains per 100 μm^2. This microstructure is reminiscent of the bimodal size distribution and abnormal grain growth that has been observed recently during annealing of dropcast nanocrystal coatings.[31] The same mechanisms described in ref 31 are likely operative here and lead to the microstructure in Figure 7f,h.

The coating compressed by hydraulic press at 800 MPa (Figure 7i) shows the highest initial coating density of the three coatings. Occasionally, holes on the surface (0.1−1 μm) of the preannealed coating can be seen. It is not clear if these voids are confined to the surface of the film or extend to the substrate, though the cross-sectional SEMs look dense. After annealing, the hydraulic-pressed coatings form the densest polycrystalline films. The annealed film is 0.4 to 1 μm thick and consists of 1 to 5 μm CZTS grains (Figure 7j,l). The large grains span the entire thickness of the film, a microstructure well-suited for

solar cells similar to densely packed large-grained films that have led to high efficiency devices.[12,13]

CZTS and CZTSSe films with large grains (>1 μm) have been shown to provide the highest solar cell efficiencies independent of the synthesis approach.[12,13,35,36] It has been difficult to achieve large-grained CZTS films by annealing nanocrystal coatings in sulfur vapor.[37,38] Nevertheless, Kim et al. were able to produce polycrystalline CZTS films by annealing trioctylphosphine oxide capped CZTS nanocrystals.[39] Chen et al. achieved similar films by annealing oxide nanoparticles.[40] These films by Kim et al. and Chen et al. resulted in 3.6 and 1.47% efficient solar cells, respectively. These efficiencies are lower than the highest efficiencies achieved (9.0%) in solar cells made by annealing CZTS nanocrystal coatings in selenium to form polycrystalline CZTSSe films.[12] This efficiency discrepancy likely is in part due to the large open-current voltage deficits in CZTS devices as compared to CZTSSe devices and reflect the differences in defect concentrations in these two different types of films.[41] Suboptimal film morphologies may also be responsible for low efficiencies in CZTS solar cells made by annealing nanocrystal coatings, especially because much higher efficiencies (8.4%) have been demonstrated in solar cells that employ CZTS films synthesized using vacuum-based process.[35] Further film growth optimization studies may be able to provide insight into improving the efficiency of CZTS solar cells from nanocrystal coatings.

4. CONCLUSIONS

Aerosol-jet printing from nanocrystal dispersions followed by mechanical compaction is a promising approach for producing nanocrystal coatings in a continuous process. An additional annealing procedure can produce polycrystalline thin films from these coatings. This approach is general but demonstrated here for the specific case of forming CZTS thin films from CZTS nanocrystal dispersions. The coating morphology depends on the ratio of the aerosol transport and evaporation times, which can be manipulated via the carrier gas flow rate. When evaporation is fast compared to aerosol transport time, the aerosol mist droplets dry substantially in flight to the substrate to form nanocrystal agglomerates. These agglomerates impinge on the substrate with little solvent content. The resulting coatings are crack-free but porous. When the aerosol transport time is short, nanocrystal dispersion droplets arrive at the substrate with higher solvent content and coalesce to form wet coatings, which crack upon drying. Porous nanocrystal agglomerate coatings formed by aerosol-jet printing can be converted to dense, crack-free nanocrystal coatings through compaction. High-temperature annealing of these compacted films in sulfur vapor showed that the thin-film microstructure depends on the preannealing coating morphology, specifically, the coating density. High-density coatings formed via compaction at high pressures can be annealed in sulfur to form dense polycrystalline films comprised of large 1–5 μm grains. In contrast, less dense films result in a porous film microstructure. Optimization of the approaches described herein and careful balancing of the factors that determine the coating and thin-film morphology may lead to a continuous roll-to-roll process for the production of thin microcrystalline films suitable for solar cells.

■ ASSOCIATED CONTENT

ⓢ Supporting Information

Additional figures and descriptions (PDF). The Supporting Information is available free of charge on the ACS Publications website at DOI: 10.1021/acsami.5b02484.

■ AUTHOR INFORMATION

Corresponding Authors
*E-mail: aydil@umn.edu.
*E-mail: lfrancis@umn.edu.
Notes
The authors declare no competing financial interest.

■ ACKNOWLEDGMENTS

■ REFERENCES

(1) Hillhouse, H. W.; Beard, M. C. Solar Cells From Colloidal Nanocrystals: Fundamentals, Materials, Devices, and Economics. *Curr. Opin. Colloid Interface Sci.* **2009**, *14*, 245−259.

(2) Habas, S. E.; Platt, H. A. S.; van Hest, M. F. A. M.; Ginley, D. S. Low-Cost Inorganic Solar Cells: From Ink To Printed Device. *Chem. Rev.* **2010**, *110*, 6571−6594.

(3) Guo, Q.; Hillhouse, H. W.; Agrawal, R. Synthesis of Cu₂ZnSnS₄ Nanocrystal Ink and Its Use For Solar Cells. *J. Am. Chem. Soc.* **2009**, *131*, 11672−11673.

(4) Steinhagen, C.; Panthani, M. G.; Akhavan, V.; Goodfellow, B.; Koo, B.; Korgel, B. A. Synthesis of Cu₂ZnSnS₄ Nanocrystals For Use In Low-Cost Photovoltaics. *J. Am. Chem. Soc.* **2009**, *131*, 12554−12555.

(5) Khare, A.; Wills, A. W.; Ammerman, L. M.; Norris, D. J.; Aydil, E. S. Size Control and Quantum Confinement In Cu₂ZnSnS₄ Nanocrystals. *Chem. Commun.* **2011**, *47*, 11721−11723.

(6) Larramona, G.; Bourdais, S.; Jacob, A.; Choné, C.; Muto, T.; Cuccaro, Y.; Delatouche, B.; Moisan, C.; Péré, D.; Dennler, G. Efficient Cu₂ZnSnS₄ Solar Cells Spray Coated From a Hydro-Alcoholic Colloid Synthesized by Instantaneous Reaction. *RSC Adv.* **2014**, *4*, 14655−14662.

(7) Mitzi, D. B.; Gunawan, O.; Todorov, T. K.; Wang, K.; Guha, S. The Path Towards a High-Performance Solution-Processed Kesterite Solar Cell. *Sol. Energy Mater. Sol. Cells* **2011**, *95*, 1421−1436.

(8) Kamoun, N.; Bouzouita, H.; Rezig, B. Fabrication and Characterization of Cu₂ZnSnS₄ Thin Films Deposited by Spray Pyrolysis Technique. *Thin Solid Films* **2007**, *515*, 5949−5952.

(9) Lincot, D.; Guillemoles, J. F.; Taunier, S.; Guimard, D.; Sicx-Kurdi, J.; Chaumont, A.; Roussel, O.; Ramdani, O.; Hubert, C.; Fauvarque, J. P.; Bodereau, N.; Parissi, L.; Panheleux, P.; Fanouillere, P.; Naghavi, N.; Grand, P. P.; Benfarah, M.; Mogensen, P.; Kerrec, O. Chalcopyrite Thin Film Solar Cells by Electrodeposition. *Sol. Energy* **2004**, *77*, 725−737.

(10) Ahmed, S.; Reuter, K. B.; Gunawan, O.; Guo, L.; Romankiw, L. T.; Deligianni, H. A High Efficiency Electrodeposited Cu₂ZnSnS₄ Solar Cell. *Adv. Energy Mater.* **2012**, *2*, 253−259.

(11) Ito, K.; Nakazawa, T. Electrical and Optical Properties of Stannite-Type Quaternary Semiconductor Thin Films. *Jpn. J. Appl. Phys.* **1988**, *27*, 2094−2097.

(12) Miskin, C. K.; Yang, W.-C.; Hages, C. J.; Carter, N. J.; Joglekar, C. S.; Stach, E. A.; Agrawal, R. 9.0% Efficient Cu$_2$ZnSn(S,Se)$_4$ Solar Cells From Selenized Nanoparticle Inks. *Prog. Photovoltaics* **2014**, *23*, 654−659.

(13) Wang, W.; Winkler, M. T.; Gunawan, O.; Gokmen, T.; Todorov, T. K.; Zhu, Y.; Mitzi, D. B. Device Characteristics of CZTSSe Thin-Film Solar Cells with 12.6% Efficiency. *Adv. Energy Mater.* **2013**, *4*, 1301465.

(14) MacDonald, B. I.; Gengenbach, T. R.; Watkins, S. E.; Mulvaney, P.; Jasieniak, J. J. Solution-Processing of Ultra-Thin CdTe/ZnO Nanocrystal Solar Cells. *Thin Solid Films* **2014**, *558*, 365−373.

(15) Guo, Q.; Ford, G. M.; Hillhouse, H. W.; Agrawal, R. Sulfide Nanocrystal Inks for Dense Cu(In$_{1−x}$Ga$_x$)(S$_{1−y}$Se$_y$)$_2$ Absorber Films and Their Photovoltaic Performance. *Nano Lett.* **2009**, *9*, 3060−3065.

(16) Law, M.; Luther, J. M.; Song, Q.; Hughes, B. K.; Perkins, C. L.; Nozik, A. J. Structural, Optical, and Electrical Properties of PbSe Nanocrystal Solids Treated Thermally or with Simple Amines. *J. Am. Chem. Soc.* **2008**, *130*, 5974−5985.

(17) Panthani, M. G.; Akhavan, V.; Goodfellow, B.; Schmidtke, J. P.; Dunn, L.; Dodabalapur, A.; Barbara, P. F.; Korgel, B. A. Synthesis of CuInS$_2$, CuInSe$_2$, and Cu(In$_x$Ga$_{1−x}$)Se$_2$ (CIGS) Nanocrystal "Inks" for Printable Photovoltaics. *J. Am. Chem. Soc.* **2008**, *130*, 16770−16777.

(18) Bucherl, C. N.; Oleson, K. R.; Hillhouse, H. W. Thin Film Solar Cells From Sintered Nanocrystals. *Curr. Opin. Chem. Eng.* **2013**, *2*, 168−177.

(19) Chiu, R. C.; Garino, T. J.; Cima, M. J. Drying of Granular Ceramic Films: I, Effect of Processing Variables on Cracking Behavior. *J. Am. Ceram. Soc.* **1993**, *76*, 2257−2264.

(20) Todorov, T.; Kita, M.; Carda, J.; Escribano, P. Cu$_2$ZnSnS$_4$ Films Deposited by a Soft-Chemistry Method. *Thin Solid Films* **2009**, *517*, 2541−2544.

(21) Kaelin, M.; Rudmann, D.; Kurdesau, F.; Zogg, H.; Meyer, T.; Tiwari, A. N. Low-Cost CIGS Solar Cells by Paste Coating and Selenization. *Thin Solid Films* **2005**, *480−481*, 486−490.

(22) Tirumkudulu, M. S.; Russel, W. B. Cracking In Drying Latex Films. *Langmuir* **2005**, *21*, 4938−4948.

(23) Jasieniak, J.; MacDonald, B. I.; Watkins, S. E.; Mulvaney, P. Solution-Processed Sintered Nanocrystal Solar Cells via Layer-by-Layer Assembly. *Nano Lett.* **2011**, *11*, 2856−2864.

(24) Chernomordik, B. D.; Béland, A. E.; Trejo, N. D.; Gunawan, A. A.; Deng, D. D.; Mkhoyan, K. A.; Aydil, E. S. Rapid Facile Synthesis of Cu$_2$ZnSnS$_4$ Nanocrystals. *J. Mater. Chem. A* **2014**, *2*, 10389−10395.

(25) Werner, C.; Godlinski, D.; Zöllmer, V.; Busse, M. Morphological Influences on the Electrical Sintering Process of Aerosol Jet and Ink Jet Printed Silver Microstructures. *J. Mater. Sci.: Mater. Electron.* **2013**, *24*, 4367−4377.

(26) Zhao, D.; Liu, T.; Park, J. G.; Zhang, M.; Chen, J.-M.; Wang, B. Conductivity Enhancement of Aerosol-Jet Printed Electronics by Using Silver Nanoparticles Ink with Carbon Nanotubes. *Microelectron. Eng.* **2012**, *96*, 71−75.

(27) Hoey, J. M.; Lutfurakhmanov, A.; Schulz, D. L.; Akhatov, I. S. A Review on Aerosol-Based Direct-Write and Its Applications for Microelectronics. *J. Nanotechnol.* **2012**, *2012*, 1−22.

(28) Mette, A.; Richter, P.; Hörteis, M.; Glunz, S. W. Metal Aerosol Jet Printing for Solar Cell Metallization. *Prog. Photovoltaics* **2007**, *15*, 621−627.

(29) Yang, C.; Zhou, E.; Miyanishi, S.; Hashimoto, K.; Tajima, K. Preparation of Active Layers in Polymer Solar Cells by Aerosol Jet Printing. *ACS Appl. Mater. Interfaces* **2011**, *3*, 4053−4058.

(30) Mahajan, A.; Frisbie, C. D.; Francis, L. F. Optimization of Aerosol Jet Printing for High-Resolution, High-Aspect Ratio Silver Lines. *ACS Appl. Mater. Interfaces* **2013**, *5*, 4856−4864.

(31) Chernomordik, B. D.; Béland, A. E.; Deng, D. D.; Francis, L. F.; Aydil, E. S. Microstructure Evolution and Crystal Growth in Cu$_2$ZnSnS$_4$ Thin Films Formed by Annealing Colloidal Nanocrystal Coatings. *Chem. Mater.* **2014**, *26*, 3191−3201.

(32) Johnson, M.; Baryshev, S. V.; Thimsen, E.; Manno, M.; Zhang, X.; Veryovkin, I. V.; Leighton, C.; Aydil, E. S. Alkali-Metal-Enhanced Grain Growth in Cu$_2$ZnSnS$_4$ Thin Films. *Energy Environ. Sci.* **2014**, *7*, 1931−1938.

(33) Sen, D.; Mazumder, S.; Melo, J. S.; Khan, A.; Bhattacharya, S.; D'Souza, S. F. Evaporation Driven Self-Assembly of a Colloidal Dispersion during Spray Drying: Volume Fraction Dependent Morphological Transition. *Langmuir* **2009**, *25*, 6690−6695.

(34) Halme, J.; Saarinen, J.; Lund, P. Spray Deposition and Compression of TiO$_2$ Nanoparticle Films for Dye-Sensitized Solar Cells on Plastic Substrates. *Sol. Energy Mater. Sol. Cells* **2006**, *90*, 887−899.

(35) Shin, B.; Gunawan, O.; Zhu, Y.; Bojarczuk, N. A.; Chey, S. J.; Guha, S. Thin Film Solar Cell with 8.4% Power Conversion Efficiency Using an Earth-Abundant Cu$_2$ZnSnS$_4$ Absorber. *Prog. Photovoltaics* **2013**, *21*, 72−76.

(36) Guo, Q.; Ford, G. M.; Yang, W.-C.; Walker, B. C.; Stach, E. A.; Hillhouse, H. W.; Agrawal, R. Fabrication of 7.2% Efficient CZTSSe Solar Cells Using CZTS Nanocrystals. *J. Am. Chem. Soc.* **2010**, *132*, 17384−17386.

(37) Tian, Q.; Xu, X.; Han, L.; Tang, M.; Zou, R.; Chen, Z.; Yu, M.; Yang, J.; Hu, J. Hydrophilic Cu$_2$ZnSnS$_4$ Nanocrystals for Printing Flexible, Low-Cost and Environmentally Friendly Solar Cells. *CrystEngComm* **2012**, *14*, 3847−3850.

(38) Gu, E.; Yan, C.; Liu, F.; Liu, Y.; Su, Z.; Zhang, K.; Chen, Z.; Li, J.; Liu, Y. Cu$_2$ZnSnS$_4$ Thin Film Solar Cells From Coated Nanocrystals Ink. *J. Mater. Sci.: Mater. Electron.* **2015**, *26*, 1932−1939.

(39) Kim, Y.; Woo, K.; Kim, I.; Cho, Y. S.; Jeong, S.; Moon, J. Highly Concentrated Synthesis of Copper-Zinc-Tin-Sulfide Nanocrystals with Easily Decomposable Capping Molecules for Printed Photovoltaic Applications. *Nanoscale* **2013**, *5*, 10183−10188.

(40) Chen, G.; Yuan, C.; Liu, J.; Huang, Z.; Chen, S.; Liu, W.; Jiang, G.; Zhu, C. Fabrication of Cu$_2$ZnSnS$_4$ Thin Films Using Oxides Nanoparticles Ink for Solar Cell. *J. Power Sources* **2015**, *276*, 145−152.

(41) Gershon, T.; Lee, Y. S.; Mankad, R.; Gunawan, O.; Gokmen, T.; Bishop, D.; McCandless, B.; Guha, S. The Impact of Sodium on the Sub-Bandgap States in CZTSe and CZTS. *Appl. Phys. Lett.* **2015**, *106*, 123905.